

A Reconfigurable Antenna With Beam Steering and Beamwidth Variability for Wireless Communications

Md. Asaduzzaman Towfiq, *Student Member, IEEE*, Israfil Bahceci[✉], *Member, IEEE*, Sebastián Blanch, Jordi Romeu[✉], *Fellow, IEEE*, Lluís Jofre, *Fellow, IEEE*, and Bedri A. Cetiner[✉], *Senior Member, IEEE*

Abstract—A reconfigurable antenna (RA) capable of steering its beam into the hemisphere corresponding to $\theta \in \{-40^\circ, 0^\circ, 40^\circ\}$, $\phi \in \{0^\circ, 45^\circ, 90^\circ, -45^\circ\}$, and of changing 3 dB beamwidth, where $\theta_{3\text{dB}} \in (40^\circ, 100^\circ)$, $\phi \in \{45^\circ, 90^\circ, -45^\circ\}$ for broadside direction is presented. The RA operating in 5 GHz band consists of a driven patch antenna with a parasitic layer placed above it. The upper surface of the parasitic layer has two pixelated metallic strips, where each strip has four pixels. The pixels connected via p-i-n diode switches enable to change the current distribution on the antenna providing the desired modes of operation. A prototype RA was characterized indicating an average gain of 8 dB. Measured and simulated impedance and radiation patterns agreed well. The proposed RA offers an efficient solution by using less number of switches compared to other RAs. The system level simulations for a 5G orthogonal frequency division multiple access system show that the RA improves capacity/coverage tradeoff significantly, where the RA modes and users are jointly determined to create proper beamwidth and directivity at the access point antennas. For a hotspot scenario, the presented RA provided 29% coverage and 16% capacity gain concurrently.

Index Terms—Antenna diversity, antenna radiation patterns, beam steering, parasitic antennas, reconfigurable antennas (RAs).

I. INTRODUCTION

INCREASING demand for high data rate and extreme broadband wireless services along with scarcity of frequency spectrum and explosive user growth have prompted the researchers to explore suitable methodologies to optimize

Manuscript received October 24, 2017; revised April 26, 2018; accepted June 25, 2018. Date of publication July 12, 2018; date of current version October 4, 2018. This work was supported in part by AFOSR under Grant FA 9550-15-1-0040DEF, in part by the Defense University Research Instrumentation Program (DURIP) under Grant FA9550-16-1-0352, in part by the Spanish Inter-Ministerial Commission on Science and Technology (CICYT) under Project TEC2016-78028-C3-1-P, and in part by FEDER and the Unidad de Excelencia María de Maeztu MDM-2016-0600, which is financed by the Agencia Estatal de Investigación, Spain. (*Corresponding author: Bedri A. Cetiner*)

Md. A. Towfiq and B. A. Cetiner are with the Department of Electrical and Computer Engineering, Utah State University, Logan, UT 84322 USA and also with i5 Technologies, Inc., North Logan, UT 84341 USA (e-mail: aztowfiq@aggiemail.usu.edu; bedri.cetiner@usu.edu).

I. Bahceci is with Ericsson Canada, Inc., Ottawa, ON K2K2R9, Canada (e-mail: israfil.bahceci@ericsson.com).

S. Blanch, J. Romeu, and L. Jofre are with the AntennaLab Research Group, Department of Signal Theory and Communications, Universitat Politècnica de Catalunya, 08034 Barcelona, Spain (e-mail: romeu@tsc.upc.edu; jofre@tsc.upc.edu).

Color versions of one or more of the figures in this paper are available online at <http://ieeexplore.ieee.org>.

Digital Object Identifier 10.1109/TAP.2018.2855668

the use of the wireless medium. Reconfigurable antennas (RAs) capable of dynamically changing their properties, e.g., radiation pattern, operational frequency, and polarization, have received a great deal of attention [1]–[12]. In particular, the RAs with radiation pattern reconfigurability help improve the system performance [13], communication security, and energy efficiency by directing signals toward the intended directions while reducing interference in unintended directions [14]. The gains with RA systems are typically achieved at the cost of increased structural (or hardware) and algorithmic (or software) complexities as compared to a legacy single-function antenna system. Therefore, it is critical to design and implement an RA equipped communication system where the hardware and software complexities are kept at minimal, and this is the main motivation behind this paper. An RA system that is capable of joint beam steering and beamwidth control enables the network to respond to spatial user variations in a dynamical manner, which is prominent for many 5G use case scenarios [15]. In particular, hotspot and ultradense deployment, and the associated spatiotemporal user and traffic variations for typical 5G technologies [16]–[18] require the radio access network to dynamically control its coverage area [19]–[21]. The RA of this paper facilitates the creation of a multitude of element radiation patterns that can be used to reshape the coverage area as desired in accordance with the network and channel variations.

There are a number of approaches for accomplishing antenna reconfigurability [22]–[32]. The approach adopted in [30]–[32] provides an efficient solution by separating the driven antenna from a reconfigurable parasitic layer. In [30], a reconfigurable parasitic pixel layer placed in the near field of the driven antenna is utilized to change the reactive loading with nine different beam steering modes. This paper introduced a relatively simple method for pattern reconfiguration, albeit with a large number of switches (e.g., at least 12 p-i-n diodes) resulting in manufacturing complexity and reduced antenna gain due to the ohmic losses of diodes. Another approach to control antenna pattern is to employ partially reflective surface (PRS) in the vicinity of a driven antenna. It is shown in [33]–[35] that the beamwidth of the antennas employing PRSs can be dynamically controlled by changing the reflective properties of the surface. These antennas offer high gain at the cost of using a large number of varactor diodes to tune the surface impedance. While several designs exist for beam steering, a few studies have been carried out to perform

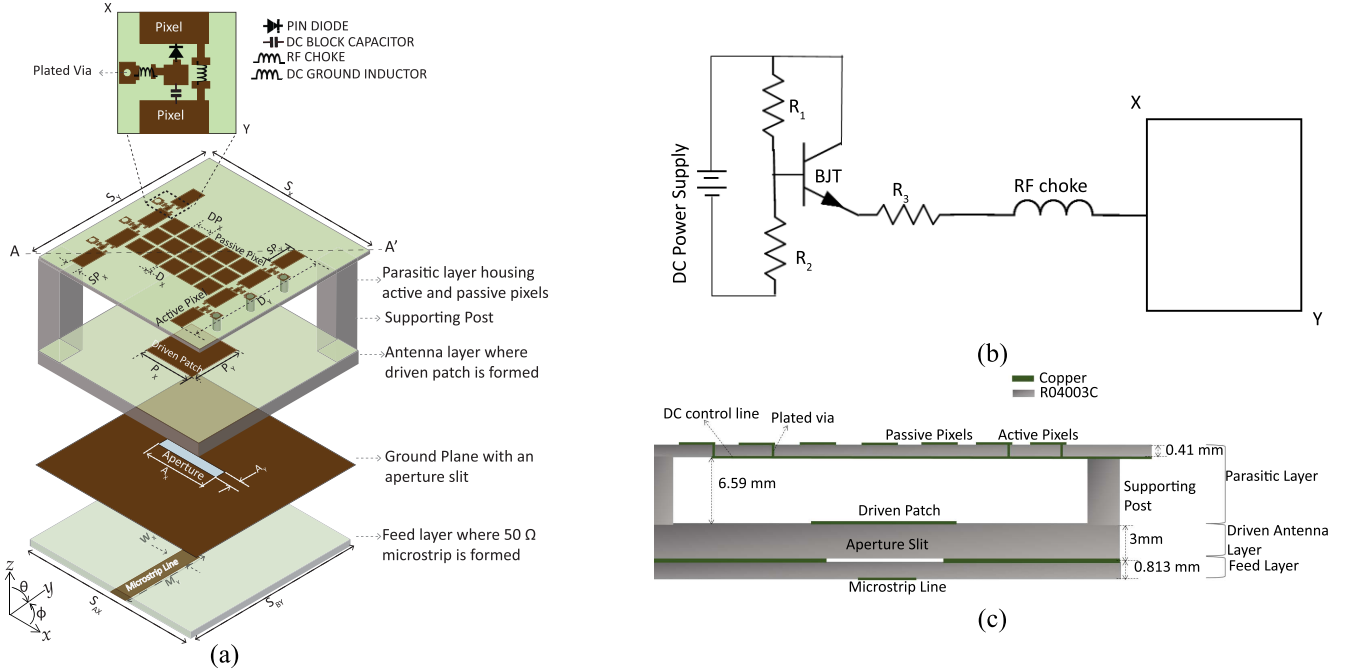


Fig. 1. (a) 3-D exploded view of the RA. (b) DC biasing scheme of the p-i-n diode. (c) AA' plane cross section of the RA.

beam steering and beamwidth variability simultaneously on a single-antenna architecture [9], [36], [37].

The RA presented in this paper employs a structure similar to the one in [30], and is capable of both beam steering and beamwidth control while requiring a small number of switches, where only six switches are used. This RA can steer its main beam into nine different directions and achieve three distinct 3 dB beamwidths in three planes corresponding to a total of 12 modes of operation. In addition, this paper proposes to use the RA in conjunction with a practical mode selection and user scheduling scheme that enables this RA for use in 3rd Generation Partnership Project (3GPP) 5G and beyond cellular access where orthogonal frequency division multiple access (OFDMA) is employed at 5 GHz band [38], [39]. For example, system level simulations assuming 5G urban micro deployment scenarios indicates that the presented RA, when used at the access points (APs), can provide up to 29% coverage gain and 16% capacity gains at the same time. The presented RA architecture (hardware) along with its control algorithm (software) enabling to choose the optimal modes of operation (the 3 dB beamwidth and beam steering direction) with respect to the dynamically changing spatial user deployments are designed and implemented with minimal hardware and software complexities, and this is the main novelty of this paper.

II. ANTENNA STRUCTURE AND WORKING MECHANISM

A. Geometry of the Antenna System

The RA, the schematics of which are shown in Fig. 1, consists of three main layers, namely feed, driven antenna (aperture coupled patch), and parasitic layers. Aperture coupled antenna offers a relatively broad bandwidth and a high degree of freedom in impedance tuning [40]. The radiating

patch is placed on the top surface of the antenna layer, where a microstrip line with $50\ \Omega$ characteristic impedance and a ground plane with an etched aperture slit are formed on the bottom and top surfaces of the feed layer, respectively. Both antenna and feed layers use Rogers R04003C substrate [41], which has been chosen for its mechanical robustness (tensile strength = 139 MPa), low cost and good electrical properties ($\epsilon_0 = 3.55$, $\tan \delta = 0.0027$). The desired band of operation has been achieved by jointly optimizing the driven patch, size, and position of the aperture, the stub length (microstrip line extension beyond aperture) and substrates' thicknesses.

The parasitic layer structure, which is formed by a RO4003C substrate of 0.41 mm thickness supported by four vertical posts with 6.59 mm thickness at its four corners, is placed on top of the driven antenna layer. The main role of this structure is to provide a mechanical support for the parasitic layer, where the 6.59 mm air gap underneath acts as a low loss medium. The upper surface of the parasitic layer has two pixelated metallic strips where each strip comprises four equally spaced rectangular metallic pixels (active pixels). The metallic strips are placed symmetrically with respect to the center of the driven patch. A grid of 3×5 square metallic pixels (passive pixels), which are not interconnected, is placed between the two pixel strips. This pixel grid acts as PRS [33] whose surface impedance reduces the reactive component of input impedance in the driven antenna, and thereby improving the impedance matching of the RA. The multiple reflections resulting from the PRS increase the gain of the RA in the broadside direction. In terms of beam steering, the variation of current distribution over the passive pixels of the PRS surface is negligible when the active pixels are connected/disconnected by turning ON/OFF the p-i-n diodes. Therefore the PRS surface does not play any significant role in steering the main beam.

TABLE I
CRITICAL DESIGN PARAMETERS (IN Millimeters)

Variable	Value	Variable	Value
(S_X, S_Y)	(60,67)	(P_X, P_Y)	(12.8,12.8)
(SP_X, SP_Y)	(4,8)	DP_X	6
(D_X, D_Y)	(1,42)	W_X	1.82
(A_X, A_Y)	(10,0.8)	(S_{AX}, S_{BY})	(60,60)
M_Y	6.5		

TABLE II
CAPACITANCE/INDUCTANCE/RESISTANCE VALUES AND SELF-RESONANT FREQUENCIES (SRFs) OF THE LUMPED COMPONENTS USED IN THE RA

Component Type	Model	Value	SRF
PIN Diode	MA4AGFCP910	N/A	N/A
RF Choke	LQW15AN15NGOOD	15 nH	5 GHz
DC grounding inductor	LQW15AN39NHOOD	39 nH	5 GHz
DC block capacitor	GOM1885C2A1R6BB01D	1.3 pF	5 GHz
Bipolar Junction Transistor (BJT)	2N3904	N/A	N/A
Resistor (R_1)	N/A	$9.83 k\Omega$	N/A
Resistor (R_2)	N/A	$50.7 k\Omega$	N/A
Resistor (R_3)	N/A	384Ω	N/A

of the RA. Pixel size and interpixel separation have been optimized to obtain high gain and improved matching for radiation in the broadside direction.

The rectangular metallic pixels in each strip are connected via p-i-n diode switches, which are controlled by dc voltages applied through control lines placed on the bottom surface of the parasitic substrate. The plated vertical vias, which run through the parasitic substrate, connect the control lines on the bottom surface to the p-i-n diode switches on the top surface. The typical biasing mechanism of the RAs has been explained in detail in our previous works [4], [30]. As shown in the magnified section of Fig. 1(a), a dc grounding inductor has been placed between each pair of adjacent pixels to provide a common dc ground for the interconnecting p-i-n diode. To ensure proper RF and dc isolation, a dc blocking capacitor has been used between the p-i-n diode and the dc-grounded pixel. RF chokes have also been used in the bias lines to minimize RF current and, hence, undesired mutual coupling effects of the bias lines with the radiating element. The complete bias circuit for the p-i-n diode is shown in Fig. 1(b), which was designed to provide a constant 10 mA current to the p-i-n diode at 1.3 V while in ON state.

An electromagnetic (EM) full-wave analysis tool [42] was used to determine the geometrical dimensions of the overall structure and surface mount device (SMD) component values resulting in the desired beam steering and beamwidth variability capabilities. The critical geometrical dimensions and the manufacturer details of the SMD components are provided in Tables I and II.

B. Working Mechanism

The working mechanism of the RA can be explained based on the classical Yagi–Uda principle [43]–[45], where the EM energy is coupled from driven element through space into

parasitic dipoles resulting in a directional beam. A microstrip Yagi antenna capable of tilting its main beam away from broadside direction, where a driven patch antenna and parasitically coupled reflector and director patches are all placed in the same horizontal plane, was developed [46].

In the presented RA, a driven patch antenna is mutually coupled with two reconfigurable pixelated parasitic strips that are placed above the driven element, with vertical distance between driven antenna layer and parasitic layer being 0.12λ at 5 GHz (as shown in Figs. 2 and 3). Since a patch antenna radiates primarily in its broadside direction, this configuration increases the energy coupling with the parasitic elements. The effective electrical lengths of the parasitic strip elements are changed by switching ON/OFF the interconnecting p-i-n diodes, making them to act either reflector or director, thus beam steering is obtained. Similar to the case of wire antennas, a parasitic patch element with slightly longer length compared to the resonant element acts as a reflector while that with slightly shorter length acts as director [46]. The parasitic element acting as director or reflector presents capacitive or inductive effect, respectively, which changes the phases of the surface current densities on the parasitic and driven elements. This phase difference causes the main beam of the RA to be steered away from its broadside direction.

Based on the above-mentioned basic EM principles, the total far-field radiation pattern of the RA structure shown in Fig. 2(a) can be expressed as [47]

$$F_a(\theta) = F_1(\theta) + \frac{I_2}{I_1} F_2(\theta) e^{-jk_0d \sin(\theta)} \left[1 - \frac{h \cot(\theta)}{d} \right] + \frac{I_3}{I_1} F_3(\theta) e^{-jk_0d \sin(\theta)} \left[1 + \frac{h \cot(\theta)}{d} \right]. \quad (1)$$

In (1), I_n , $n = 1, 2$ and 3 , is the complex current value for element n and k_0 is the free space phase constant at 5 GHz. The lateral distance between driven and each parasitic element is $d = 20$ mm, and vertical separation between the driven antenna and parasitic layers is $h = 7$ mm. The field pattern of the RA elements in isolation can be approximated using the radiation pattern of a typical patch antenna [48], where $F_i(\theta)$ for $i = 1, 2, 3$ are given as follows:

$$F_1(\theta) = \cos(\theta) \frac{\sin \left[\frac{k_0 W_d}{2} \sin(\theta) \right]}{\frac{k_0 W_d}{2} \sin(\theta)} \quad (2)$$

$$F_2(\theta) = F_3(\theta) = \cos(\theta) \frac{\sin \left[\frac{k_0 W_p}{2} \sin(\theta) \right]}{\frac{k_0 W_p}{2} \sin(\theta)}. \quad (3)$$

In (2) and (3), the widths of the driven patch and parasitic element are $W_d = 13$ and $W_p = 6$ mm, respectively. The design parameters W_d , W_p , d , and h are jointly optimized to perform effective beam steering in the targeted 5 GHz band. The range for θ angle is, $0^\circ < \theta < 180^\circ$.

The complex currents, I_n , $n = 1, 2$, and 3 , are calculated by integrating the magnetic fields H_1 , H_2 , and H_3 along the closed curves C_1 , C_2 , and C_3 containing element surfaces as shown in Fig. 2(a). Calculated current ratios for obtaining the radiation patterns, as shown in Fig. 2(b) and (c), corresponding

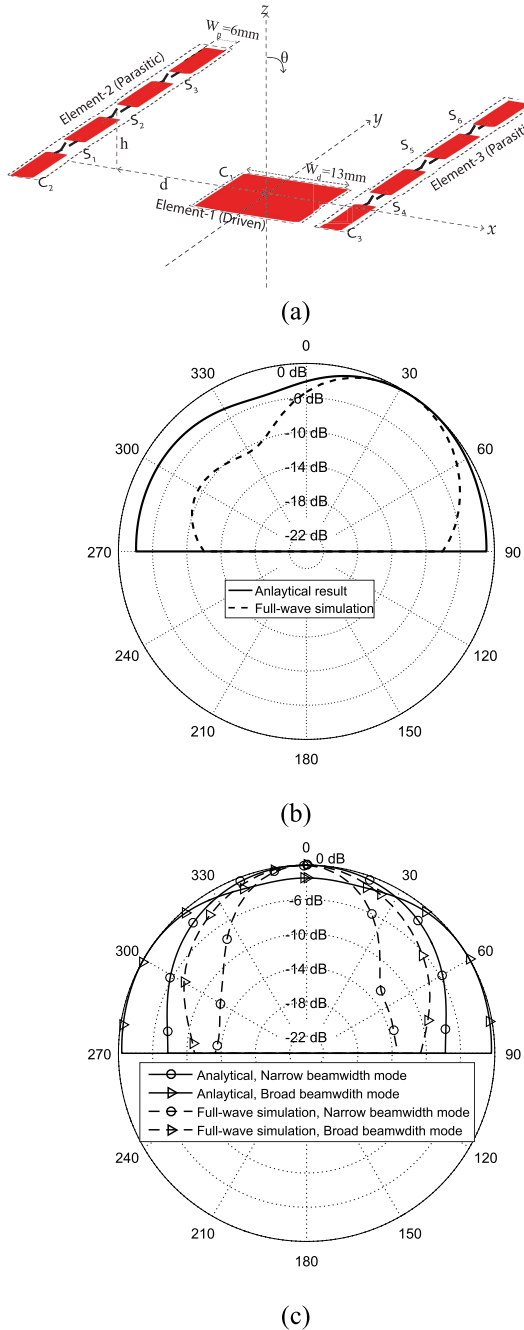


Fig. 2. (a) RA structure consisting of driven and parasitic elements. C_i denotes the curve enclosing element- i , for $i = 1, 2, 3$. S_i for $i = 1, 2 \dots 6$ denotes the interconnecting RF switches. (b) Field patterns corresponding to beam steering in xz plane obtained by analytic method and full-wave simulation (S_1, S_2, S_3 are ON and S_4, S_5, S_6 are OFF). (c) Field patterns for beamwidth variability in yz plane obtained by analytic method and full-wave simulation.

to beam steering and different beam widths, respectively, are as follows.

- 1) $(I_2/I_1) = 0.8e^{-j1.7}$ and $|I_3/I_1| \approx 0$ for beam steering.
- 2) $(I_2/I_1) = (I_3/I_1) = 0.8e^{-j1.7}$ for beamwidth variability.

Fig. 2(b) and (c) shows that the approximate analytical approach for beam steering and beamwidth variability agree reasonably well with full-wave analysis results.

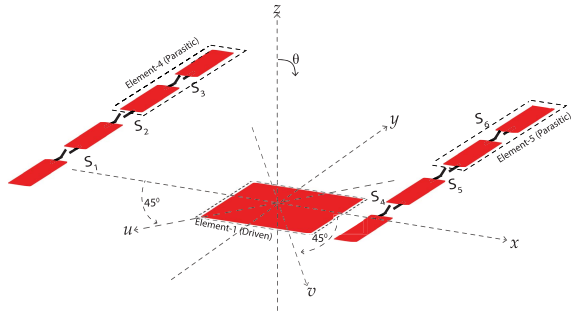


Fig. 3. RA configurations for beam steering in yz plane.

Let us use (1) and first describe the principle of beam steering in xz plane, where the beam steering in all other planes can be easily explained based on this. As depicted in Fig. 2(a), when the switches S_1, S_2 , and S_3 are turned ON, and S_4, S_5 , and S_6 are turned OFF, the effective electrical length of the element 2 becomes larger and that of element 3 becomes smaller than the length of the driven element 1. Induced currents in the parasitic elements are proportional to the effective electrical lengths, and hence $I_2 \gg I_3$. The individual size of a parasitic pixel has been optimized such that $I_3 \approx 0$. Therefore, in this case, (1) can be simplified as

$$F_a(\theta) = F_1(\theta) + \frac{I_2}{I_1} F_2(\theta) e^{-jk_0 d \sin(\theta)} \left[1 - \frac{hcot(\theta)}{d} \right]. \quad (4)$$

Equation (4) represents the total field pattern of a two-element linear array with individual element patterns of $F_1(\theta)$ and $F_2(\theta)$ and excitation currents of I_1 and I_2 . Also, notice that the array axis, on which the centers of the elements are placed, is the x -axis. The excitation currents I_1 and I_2 are complex numbers, where their ratio can be expressed as

$$\frac{I_2}{I_1} = X e^{-j\gamma} \quad (5)$$

where X is the magnitude and γ is the phase of the current ratio. By substituting (5) into (4), we obtain the following:

$$F_a(\theta) = F_1(\theta) + X F_2(\theta) e^{-jk_0 d \sin(\theta)} \left[1 - \frac{hcot(\theta)}{d} \right] - j\gamma. \quad (6)$$

While F_1 and F_2 are not identical, they have been obtained from same equation [see (2) and (3)]. Therefore, they have similar patterns, which can be taken to be approximately same, $F(\theta) = F_1(\theta) \approx F_2(\theta)$, for the ease of analysis. The parasitic elements have been optimized such that $|I_1| \approx |I_2|$, and hence $|X| \approx 1$. Now, (6) can further be simplified as

$$F_a(\theta) = F(\theta) \left(1 + e^{-jk_0 d \sin(\theta)} \left[1 - \frac{hcot(\theta)}{d} \right] - j\gamma \right). \quad (7)$$

It can be readily observed that $(1 + e^{-jk_0 d \sin(\theta)} [1 - (hcot(\theta)/d)] - j\gamma)$ in (7) is the array factor of a two-element linear array consisting of element 2 (parasitic) and element 1 (driven antenna) of which centers lie on the x -axis, which is the array axis. The beam steering is performed in the plane that contains and is orthogonal to the array axis, which is the xz plane. In (7), γ is the phase gradient that controls the steering angle of the main beam of

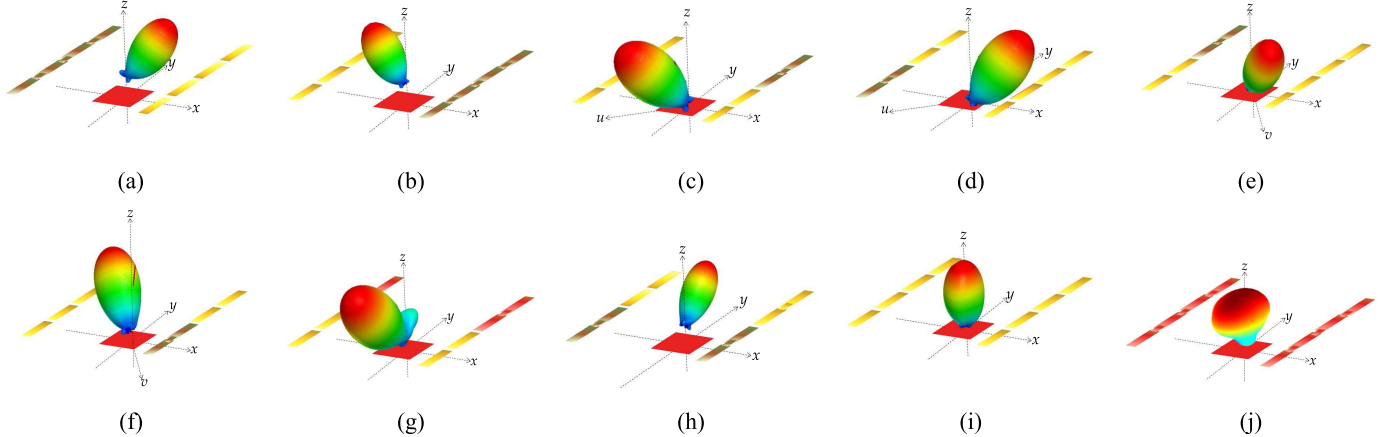


Fig. 4. Representative radiation patterns in decibel scale for beam steering toward (a) $+x$ -direction (b) $-x$ -direction (c) $+u$ -direction (d) $-u$ -direction (e) $+v$ -direction (f) $-v$ -direction (g) $-y$ -direction, and (h) $+y$ -direction, and (i) narrow and (j) broad beamwidth. Yellow colored pixels are disconnected and red colored pixels are connected.

the array, which in this case is the RA. With this analysis, it can be readily seen that while turning S_1 , S_2 , and S_3 ON, and keeping S_4 , S_5 , and S_6 in OFF state steers the beam toward $+x$ -direction, keeping S_1 , S_2 , and S_3 in OFF state, and turning S_4 , S_5 , and S_6 ON steers the beam toward $-x$ -direction. The corresponding representative radiation patterns for these cases are shown in Fig. 4(a) and (b).

By using (1)–(7), one can see that the beam steering along $+u$ - and $-u$ -axes are achieved, when the centers of array elements lie on the u -axis, i.e., the array axis is u -axis. For beam steering toward $+u$ -direction, switch S_6 is turned ON and all other switches are turned OFF, and for beam steering toward $-u$ -direction, switch S_1 is turned ON and all other switches are turned OFF. The corresponding patterns are shown in Fig. 4(c) and (d). In an analogous way, the beam steering along v -axis, i.e., toward $+v$ - and $-v$ -directions, can be explained, where the corresponding patterns are as shown in Fig. 4(e) and (f).

The beam steering along the y -axis can be achieved by creating an array geometry where the parasitic elements and the driven element are aligned along both the u - and v -axes (see Fig. 3). In this case, the resultant field pattern becomes the vector summation of the patterns along u - and v -axes, thus one can obtain a steered beam pattern along y -axis. This can be accomplished in two ways: 1) switches S_3 and S_6 are turned ON and all other switches are kept in the OFF state, thereby element 4 parasitic and element 1 driven patch are aligned along v -axis, and element 5 parasitic and element 1 driven patch are aligned along u -axis. This configuration results in beam steering toward $-y$ -direction, and 2) switches S_1 and S_4 are turned ON and all other switches are kept in the OFF state, thereby beam is steered toward $+y$ -direction. The corresponding patterns are shown in Fig. 4(g) and (h).

The 3 dB beamwidth of the presented RA can be broadened in yz plane by turning all the switches ON. In this case, the induced current magnitudes in both elements 2 and 3 become close ($|I_2/I_1| = |I_3/I_1| = 0.8$) to element 1. Elements 1, 2, and 3 form a linear array along x -axis, as shown

TABLE III
SWITCH CONFIGURATION FOR DESIRED MODES OF OPERATION
(1 = ON, 0 = OFF, (θ, ϕ) INDICATE PEAK GAIN ANGLES)

Modes	θ	θ_{3dB}	ϕ	S_1	S_2	S_3	S_4	S_5	S_6
1	0°	40°	0°	0	0	0	0	0	0
2	40°		0°	0	0	0	1	1	1
3	-40°		0°	1	1	1	0	0	0
4	40°		45°	0	0	0	0	0	1
5	-40°		45°	1	0	0	0	0	0
6	30°		90°	0	0	1	0	0	1
7	-30°		90°	1	0	0	1	0	0
8	40°		-45°	0	0	1	0	0	0
9	-40°		-45°	0	0	0	1	0	0
10	0°	100°	45°	1	0	0	0	0	1
11	0°	100°	90°	1	1	1	1	1	1
12	0°	100°	-45°	0	0	1	1	0	0

in Fig. 2(a). Due to the phase differences between the element currents, the resultant radiation pattern using (1) can be shown to broaden the 3 dB beamwidth in yz plane compared to the case where all switches are in OFF state corresponding to a patch pattern with a narrow beamwidth. The corresponding representative radiation patterns for narrow and broad beam widths are shown in Fig. 4(i) and (j), respectively.

III. PROTOTYPE CHARACTERIZATION AND NUMERICAL EXAMPLES

A. Measurement and Simulation Results

A prototype RA was fabricated based on the standard printed circuit board fabrication processes and measured to validate the theoretical analyses and simulated results. Fig. 5 shows the photograph of the RA measurement setup where the six p-i-n diode switches interconnecting the adjacent pixels are numbered in order to identify the switch status for each mode of operation. The switch configurations and associated modes of operation are shown in Table III.

The measurements included the reflection coefficients and realized gain patterns, which are cut at 5 GHz, for all 12 modes of operations. For the gain patterns, only the copol components are plotted as the cross-pol components are at least -10 dB



Fig. 5. Photograph of the RA measurement setup showing numbered interpixel p-i-n diode switches.

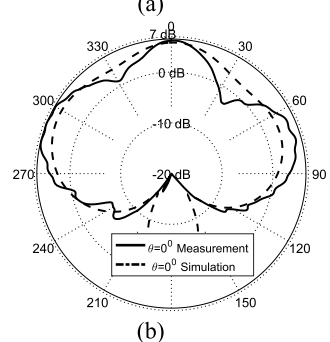
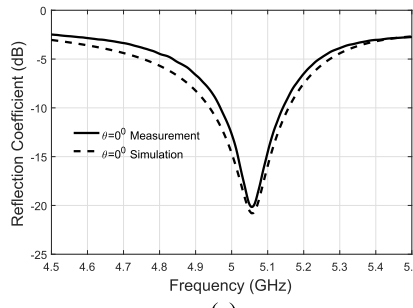


Fig. 6. Simulated and measured (a) reflection coefficients and (b) realized gain patterns of the RA for $\theta = 0^\circ$ on $\phi = 0^\circ$ plane (mode 1).

less than the copol components. The simulated and measured results for modes 1–9 are shown in Figs. 6–10 with good agreement between simulations and measurements. For all these modes, the common bandwidth covers 4.9–5.1 GHz band, and the maximum realized gain of ~ 8 dB is achieved. Fig. 11(a) shows the variations of simulated realized gains at the associated steered angles ($\theta = -40^\circ$ and 40° , for modes 2 and 3, respectively) with respect to frequency. These results demonstrate that the steered angles are maintained and gains stay reasonably flat over the entire frequency band for both modes. In Fig. 11(b), the simulated axial ratios with respect to frequency are shown for modes 2 and 3, indicating that the RA maintains linear polarization over the entire 4.9–5.1 GHz band. Other modes show similar behavior

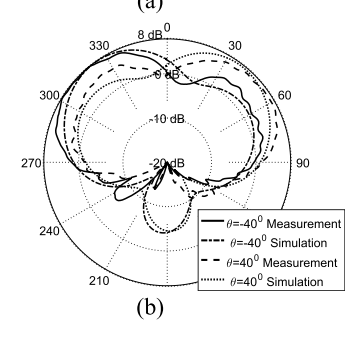
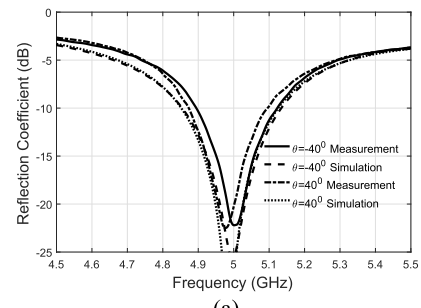


Fig. 7. Simulated and measured (a) reflection coefficients and (b) realized gain patterns of the RA for $\theta = 40^\circ$ and $\theta = -40^\circ$ on $\phi = 0^\circ$ plane (modes 2 and 3).

in terms of gain flatness and polarization purity. Fig. 11(c) shows the effect of the parasitic layer on the copol and cross-pol patterns of the RA. While the cross-pol pattern remains relatively unchanged (<−20 dB), the small reduction in the copol component can be attributed to the RF losses of the p-i-n diodes and the bias circuitry. The beamwidth variability modes, i.e., modes 10–12, are shown in Figs. 12–14, again with good agreement between simulation and measurement results. From these figures, an average of 60° increase in the 3 dB beamwidth in $\phi = 45^\circ, 90^\circ$ and, -45° planes as compared to the beamwidth of mode 1 (standard patch mode) can be observed.

The efficiency of the RA has been measured, where the efficiency with parasitic layer reduces to 81% compared to

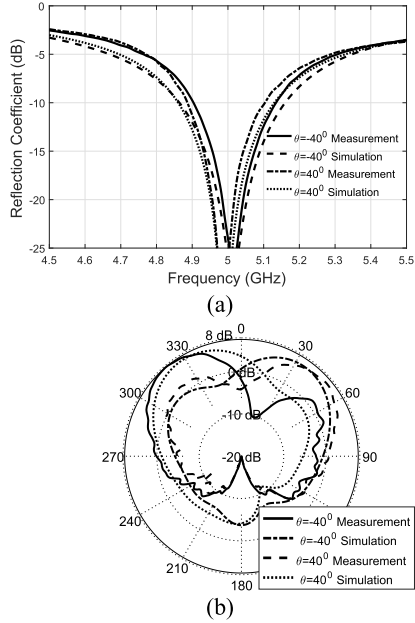


Fig. 8. Simulated and measured (a) reflection coefficients and (b) realized gain patterns of the RA for $\theta = 40^\circ$ and $\theta = -40^\circ$ on $\phi = 45^\circ$ plane (modes 4 and 5).

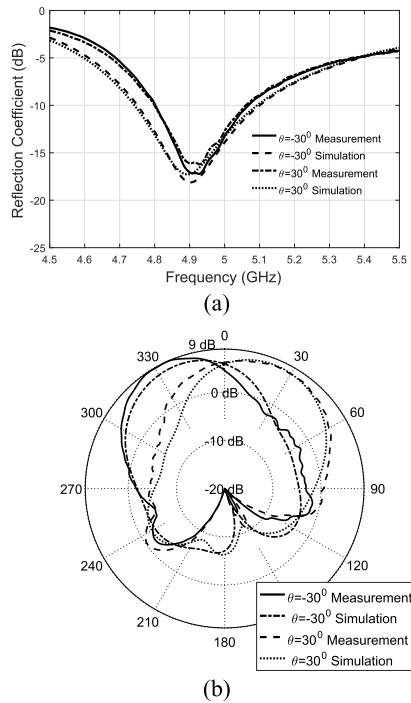


Fig. 9. Simulated and measured (a) reflection coefficients and (b) realized gain patterns of the RA for $\theta = 30^\circ$ and $\theta = -30^\circ$ on $\phi = 90^\circ$ plane (modes 6 and 7).

95% without the parasitic layer, which corresponds to the efficiency of the driven patch antenna. This reduction can be attributed to the RF losses of the p-i-n diodes, associated bias circuitry and the parasitic substrate.

B. Performance of Proposed RA in OFDMA System

The availability of multiple radiation patterns with an RA results in different signal strength coverages complicating its utilization in cellular networks. Here, we develop a method

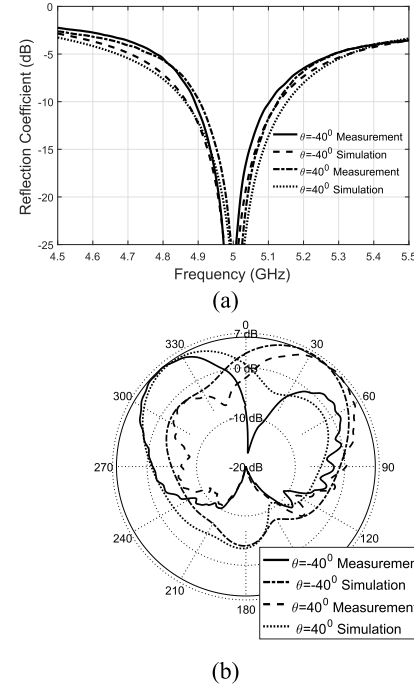


Fig. 10. Simulated and measured (a) reflection coefficients and (b) realized gain patterns of the RA for $\theta = 40^\circ$ and $\theta = -40^\circ$ on $\phi = -45^\circ$ plane (modes 8 and 9).

to utilize the proposed RA for a 5G cellular communication system employing OFDMA-based transmission. With OFDMA, selection of the RA mode (i.e., radiation pattern) in conjunction with user scheduling is critical to cultivate the frequency selective scheduling gains along with the spatial diversity provided by the RA mode optimization.

1) System Model: Assume a wireless network of N APs each with S sectors amounting to a total of NS cells. We assume that each cell is equipped with the RA that can create M different radiation patterns whose complex field is $\vec{B}_j(\theta, \phi; \mu)$ with $\mu \in \{1, \dots, M\}$ denoting the index of the RA mode at cell j . The users are randomly distributed within the cell's coverage area, and each user is equipped with a standard half-wavelength dipole antenna. Let us investigate a single cell serving L users, U_l , $l = 1, \dots, L$. Let $h_l(n, k; \mu_n)$ represent the channel gain from AP RA (with mode- μ_n) to the U_l at time t_n and frequency f_k .

We consider the OFDMA transmission scheme described in 3GPP TS 38.211 [49] with a subcarrier spacing of $\Delta_f = 15$ KHz. For resource block- b (RB- b) in a single frequency (SF) (consisting of N_{sc} subcarriers and with a duration of T_{SF} secs), the instantaneous achievable throughput (using the Shannon capacity formula) can be obtained for U_l as¹

$$r_l(b; \mu) = (1 - \delta)N_{sc}T_{SF}\Delta_f \times \frac{1}{|\mathcal{D}|} \sum_{(k,n) \in \mathcal{D}} \log_2 \left(1 + \frac{P_j \|h_l(n, k; \mu_n)\|^2}{\sigma_{k,n}^2} \right) \quad (8)$$

where $\sigma_{k,n}^2$ is the interference plus noise power at subcarrier (k, n) , P_j is the transmit power at serving cell, and

¹For brevity, we drop the SF time index.

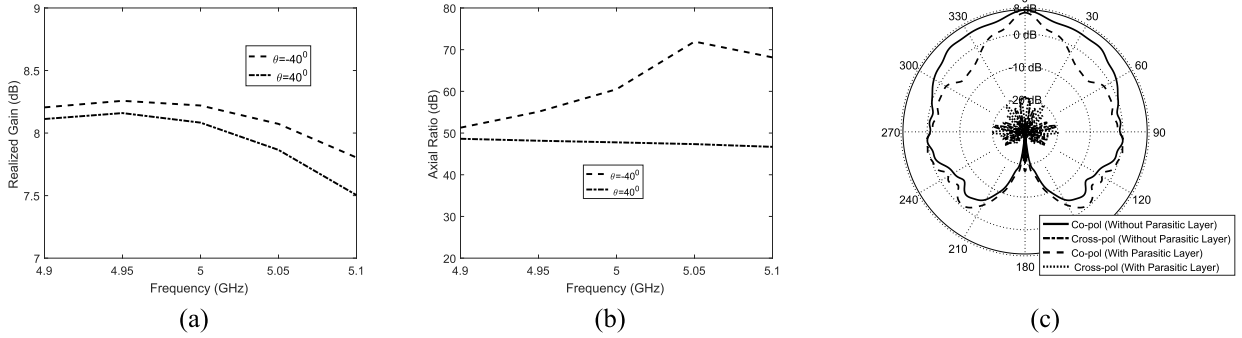


Fig. 11. For $\theta = 40^\circ$ and $\theta = -40^\circ$ on $\phi = 0^\circ$ plane (modes 2 and 3) (a) Realized gain variation and (b) axial ratio over frequency. (c) Measured Copol and Cross-pol patterns of the RA in yz plane for mode 1 at 5 GHz with and without the parasitic layer.

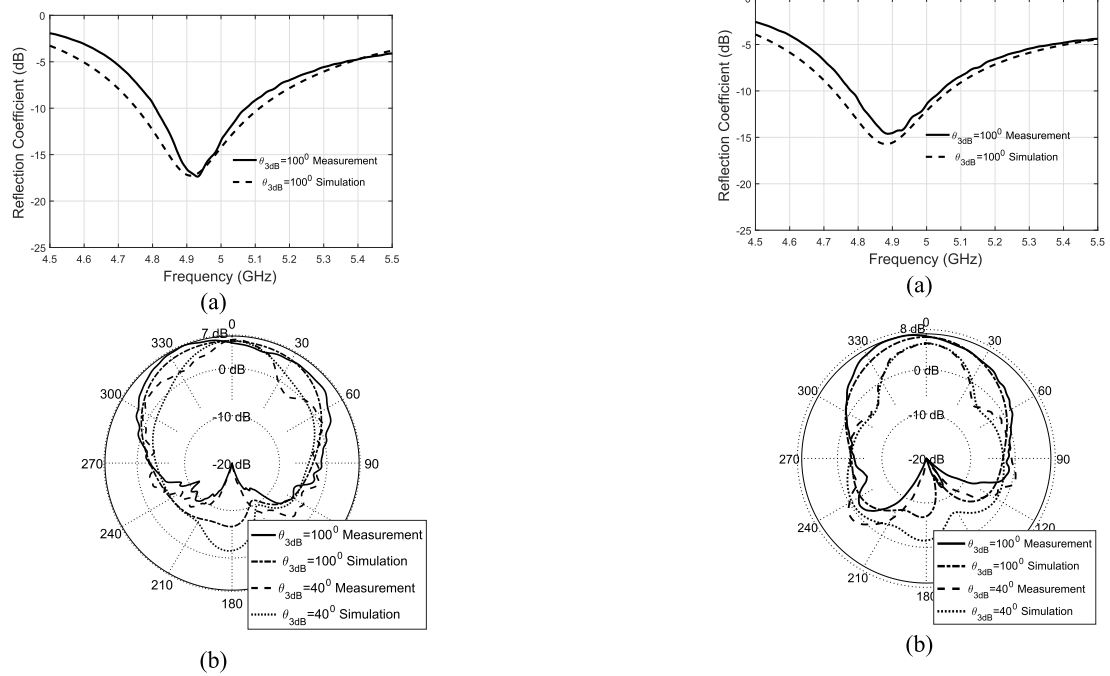


Fig. 12. Simulated and measured (a) reflection coefficients and (b) realized gain patterns of the RA for $\theta_{3dB} \in \{100^\circ, 40^\circ\}$ on $\phi = 45^\circ$ plane (mode 10).

$\delta = |\mathcal{P}|/|\mathcal{D}|$ with \mathcal{P} and \mathcal{D} denoting the set of pilot and data subcarriers in RB- b , respectively. For a fixed RA mode μ , the proportionally fair (PF) scheduler determines the user index l^* at RB- b according to

$$l^*(b; \mu) = \arg \max_{l|b, \mu} \frac{\hat{r}_l(b; \mu)}{\bar{R}_l} \quad (9)$$

where $\hat{r}_l(b; \mu)$ is the instantaneous achievable throughput estimated based on the pilot subcarriers in the RB, and \bar{R}_l is the average throughput. Note that with a fixed RA mode at the AP, the PF scheduler maximizes the sum of logarithms of the rates of the users corresponding to that mode.

2) *Mode Selection and Scheduling*: Each RA mode creates a different signal-to-noise ratio distribution, and thus, results in different long-term rates for each user. This complicates an exact derivation of the PF scheduler. Here, we develop a mode-aware modified PF scheduler that imposes a constraint

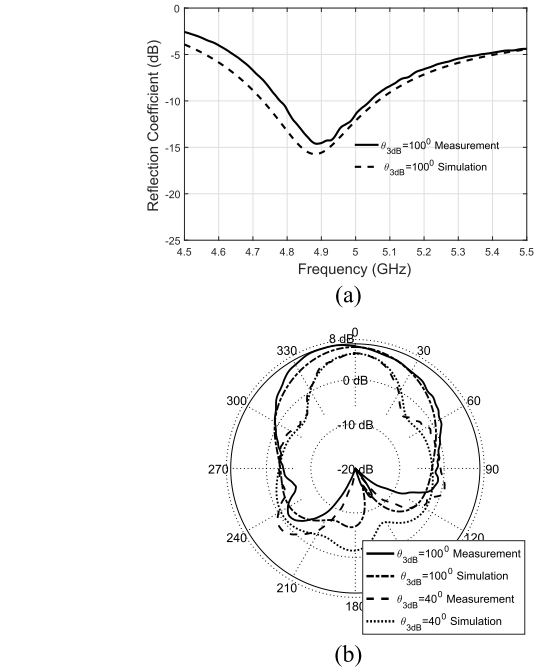


Fig. 13. Simulated and measured (a) reflection coefficients and (b) realized gain patterns of the RA for $\theta_{3dB} \in \{100^\circ, 40^\circ\}$ on $\phi = 90^\circ$ plane (mode 11).

TABLE IV
SYSTEM LEVEL SIMULATION PARAMETERS

Parameter	Value	Parameter	Value
Number of APs	19	Sectors per AP	3
AP-AP distance	250 m	AP-UE channel	UMa [50]
Average number of UEs per cell	20	UE deployment	Uniform or Hotspot
Average number of hotspots per cell	4	Number of UEs per hotspot	5
min AP-UE distance	10 m	min inter-cluster distance	50 m
Number of RA modes	12	AP Tx Power	30 dBm
Channel bandwidth	10 MHz	Number of SCs (N)	600

on the set of users enrolling in the PF prioritization. For each subframe, the AP estimates a weighted sum-rate for each mode assuming PF scheduling, and then selects the

TABLE V
COMPARISON AMONG VARIOUS RAs

Publications	No. of Modes	No. of Switches	Beam Steering	Beam Steering Range	Beam Width Variable	Pattern Purity (Cross Polarization Level)	Average Gain (dB)	Efficiency	Frequency BW (GHz)	Joint optimization of RA modes and control algorithm
[30]	9	12	Yes	$-30^\circ, 30^\circ$	No	<-10dB	6.5	N/A	2.4-2.5	Yes
[37]	N/A	100	Yes	$-10^\circ, 10^\circ$	Yes	-12dB	14.7	N/A	1.9-2.1	No
[9]	4	8	Yes	$-17^\circ, 14^\circ$	Yes	-15dB	7	N/A	3.32-3.62	No
[10]	9	4	Yes	$-22^\circ, 22^\circ$	No	N/A	7.5	76%	2.36-2.39	No
This work	12	6	Yes	$-40^\circ, 40^\circ$	Yes	<-20dB	8	81%	4.9-5.1	Yes

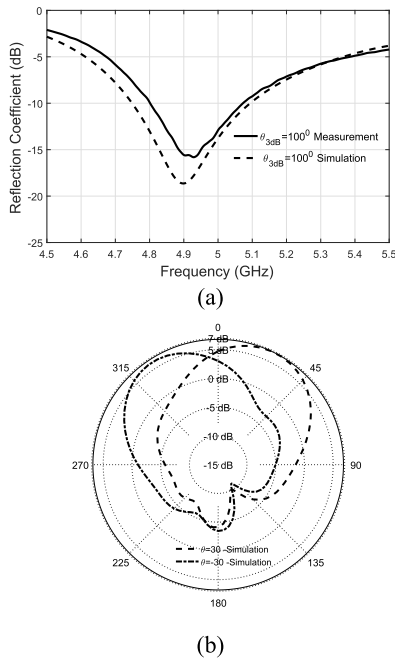


Fig. 14. Simulated and measured (a) reflection coefficients and (b) realized gain patterns of the RA for $\theta_{3\text{dB}} \in \{100^\circ, 40^\circ\}$ on $\phi = -45^\circ$ plane (mode 12).

mode (μ^*) maximizing the weighted sum-rate, that is,

$$\begin{aligned} l^*(b; \mu^*) &= \arg \max_{\mu \in \mathcal{M}} \sum_b \frac{\hat{r}_l^*(b; \mu)}{\bar{R}_l} \\ \text{s.t. } l^*(b; \mu) &= \arg \max_{l \in \mathcal{U}_\mu | b, \mu} \frac{\hat{r}_l(b; \mu)}{\bar{R}_l} \end{aligned} \quad (10)$$

where $\mathcal{U}_\mu \subseteq \mathcal{U}$ is the user subset that are allowed to be scheduled when the RA assumes mode μ . The members and size of \mathcal{U}_μ determine a tradeoff between the gains due to frequency selective scheduling and the pattern optimization. To achieve this for each mode, we propose signal strength-based subset selection scheme

$$\begin{aligned} \mathcal{U}_\mu &\triangleq \{l : \mu \in \mathcal{M}_l\} \\ \text{s. t. } \mathcal{M}_l &\triangleq \left\{ \mu : \frac{g_l(\mu)}{\max_\mu g_l(\mu)} \geq g_{\text{th}}, \quad l = 1, \dots, L \right\} \end{aligned} \quad (11)$$

where $g_l(\mu) = E_n \{ \sum_k \|h_l(n, k; \mu)\|^2 \}$ is the average channel power for U_l , and $g_{\text{th}} \in [0, 1]$ is a threshold parameter controlling the cardinality of \mathcal{U}_μ . Note that this scheme

first determines the set of suitable RA modes for each user (e.g., modes that can provide acceptable signal quality to the user), and then for each mode, aggregates the users that can be served by that mode. This approach ensures that each user can be served using at least one RA mode when $g_{\text{th}} > 0$, and by any of the modes when $g_{\text{th}} = 0$.

3) *Numerical Examples*: System level simulation parameters for the network are provided in Table IV. Two spatial user deployments are studied: 1) uniform user density where users are dropped uniformly within the coverage area and 2) hotspot deployment where users are dropped within 20 m of cluster centers that are spatially randomly distributed.

Performance is analyzed for three cases: APs employ 1) legacy patch antennas; 2) RAs where UEs report the strongest mode; and 3) RAs where UEs report modes having signal strength within 3 dB of the strongest mode. Fig. 15(a) compares the radiation patterns for various RA modes and the patch antenna in a typical cell serving several UEs for the hotspot scenario. It is seen that the RA can provide an enhanced set of beam patterns that can be adapted to spatial UE or traffic distribution. Average capacity-coverage performance for the two deployment cases is illustrated in Fig. 15(b). The coverage is defined as the 5 percentile of the cumulative distribution function (CDF) of per-user rates. It is seen that for both deployment scenarios, the RA system achieves superior capacity/coverage tradeoff against the system using legacy patch antennas. For example, the RA system can provide up to 29% coverage/16% capacity improvement for hotspot scenario and up to 25% coverage/14% capacity improvement for the case of uniform user distribution. The improvements are pronounced more for hotspot scenarios as beam steering and beamwidth control can provide better signal coverage to the hotspot areas while maintaining lower interference to unintended users. The results with $g_{\text{th}} = 0$ indicates that when a user is served with the RA mode providing the strongest signal quality (e.g., corresponding to activation of average four modes in each cell under the studied scenarios), the system can achieve significant improvements. In this case, the gains are mainly due to the pattern control offered by the RA. With lower g_{th} values, the gains from multiuser diversity is enhanced for each RA mode, and along with the gains from RA pattern diversity, further improvement is obtained.

A comparison between the presented RA and similar other RAs in terms of the number of modes generated, number of switches used, and RA properties such as beam steering

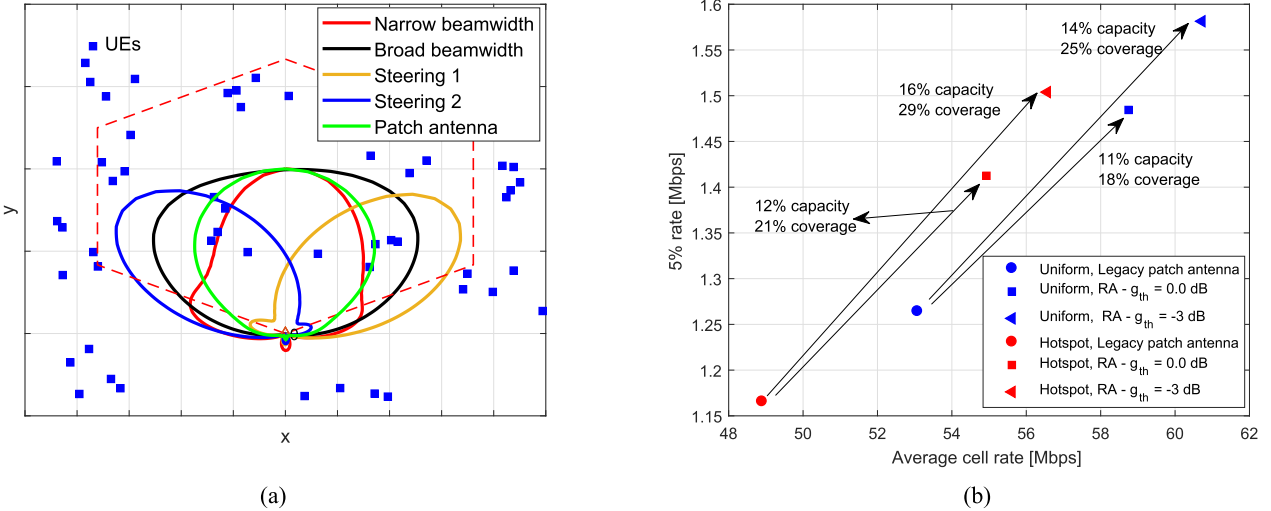


Fig. 15. (a) Radiation patterns for various RA modes and the patch antenna in a typical cell. (b) Throughput-coverage performance of RA and the legacy patch antenna for two use cases, Uniform and Hotspot.

capability, beamwidth variability, pattern purity, average gain, etc., is given in Table V. It can be observed that the RA of this paper is advantageous for achieving larger number of modes per the number of switches used. In particular, compared to [30], this RA does not only provide larger number of modes with less number of switches, greater beam steering range, and better pattern purity but also the average antenna gain, which is 8 dB, is increased by ~ 1.5 dB. Note that the largest average gain of 14.7 dB for work presented in [37] uses a 1×2 antenna array as its driven element, thereby having a complex driven antenna structure. While this paper achieves analog beam steering with a range of $\sim 20^\circ$ and small beamwidth variability, the 1×2 array structure with phase shifters and the PRS with exceedingly large number of varactors and associated biasing circuitry results in very complex antenna structure and high RF losses. Another significant advantage of the RA presented in this paper compared to the ones given in Table V is that the proposed control algorithm enables to choose the optimal modes of operation (the 3 dB beamwidth and beam steering direction) in an efficient way with respect to the dynamically changing spatial user deployments.

IV. CONCLUSION

A new parasitic coupling-based RA design that can provide beam steering and beamwidth control on a single compact antenna platform is developed. The proposed RA can generate nine beam steering and three beamwidth variable modes. With a novel RA mode-aware PF scheduling scheme that jointly determines the RA pattern and scheduled users, the proposed RA can provide significant improvements against the system using legacy patch antennas, e.g., up to 29% coverage and 16% throughput gains for a hotspot scenario. The improvements are critical for 5G wireless access where extreme broadband along with ubiquitous coverage is mandated by the 5G requirements. The presented RA architecture (hardware) along with its control algorithm (software) enabling to choose the optimal modes of operation (the 3 dB beamwidth and beam

steering direction) with respect to the dynamically changing spatial user deployments are designed and implemented with minimal hardware and software complexities. We conclude that designing RAs in conjunction with signaling schemes and network requirements with low overhead is essential to optimize overall system performance.

REFERENCES

- [1] D. Rodrigo, B. A. Cetiner, and L. Jofre, "Frequency, radiation pattern and polarization reconfigurable antenna using a parasitic pixel layer," *IEEE Trans. Antennas Propag.*, vol. 62, no. 6, pp. 3422–3427, Jun. 2014.
- [2] Z. Li, D. Rodrigo, L. Jofre, and B. A. Cetiner, "A new class of antenna array with a reconfigurable element factor," *IEEE Trans. Antennas Propag.*, vol. 61, no. 4, pp. 1947–1955, Apr. 2013.
- [3] C. J. Panagamuwa, A. Chauraya, and J. C. Vardaxoglou, "Frequency and beam reconfigurable antenna using photoconducting switches," *IEEE Trans. Antennas Propag.*, vol. 54, no. 2, pp. 449–454, Feb. 2006.
- [4] D. Rodrigo, J. Romeu, B. A. Cetiner, and L. Jofre, "Pixel reconfigurable antennas: Towards low-complexity full reconfiguration," in *Proc. 10th Eur. Conf. Antennas Propag. (EuCAP)*, Apr. 2016, pp. 1–5.
- [5] A. Zohur, H. Mopidevi, D. Rodrigo, M. Unlu, L. Jofre, and B. A. Cetiner, "RF MEMS reconfigurable two-band antenna," *IEEE Antennas Wireless Propag. Lett.*, vol. 12, pp. 72–75, 2013.
- [6] M. W. Young, S. Yong, and J. T. Bernhard, "A miniaturized frequency reconfigurable antenna with single bias, dual varactor tuning," *IEEE Trans. Antennas Propag.*, vol. 63, no. 3, pp. 946–951, Mar. 2015.
- [7] A. J. King, J. F. Patrick, N. R. Sottos, S. R. White, G. H. Huff, and J. T. Bernhard, "Microfluidically switched frequency-reconfigurable slot antennas," *IEEE Antennas Wireless Propag. Lett.*, vol. 12, pp. 828–831, 2013.
- [8] S. V. Hum and J. Perruisseau-Carrier, "Reconfigurable reflectarrays and array lenses for dynamic antenna beam control: A review," *IEEE Trans. Antennas Propag.*, vol. 62, no. 1, pp. 183–198, Jan. 2014.
- [9] W.-Q. Deng, X.-S. Yang, C.-S. Shen, J. Zhao, and B.-Z. Wang, "A dual-polarized pattern reconfigurable Yagi patch antenna for microbase stations," *IEEE Trans. Antennas Propag.*, vol. 65, no. 10, pp. 5095–5102, Oct. 2017.
- [10] M. Jusoh, T. Aboufoul, T. Sabapathy, A. Alomainy, and M. R. Kamarudin, "Pattern-reconfigurable microstrip patch antenna with multidirectional beam for wimax application," *IEEE Antennas Wireless Propag. Lett.*, vol. 13, pp. 860–863, 2014.
- [11] J. Hu, S. Lin, and F. Dai, "Pattern reconfigurable antenna based on morphing bistable composite laminates," *IEEE Trans. Antennas Propag.*, vol. 65, no. 5, pp. 2196–2207, May 2017.

- [12] N. H. Chamok, M. H. Yilmaz, A. Arslan, and M. Ali, "High-gain pattern reconfigurable MIMO antenna array for wireless handheld terminals," *IEEE Trans. Antennas Propag.*, vol. 64, no. 10, pp. 4306–4315, Oct. 2016.
- [13] B. A. Cetiner, H. Jafarkhani, J.-Y. Qian, H. J. Yoo, A. Grau, and F. D. Flaviis, "Multifunctional reconfigurable MEMS integrated antennas for adaptive MIMO systems," *IEEE Commun. Mag.*, vol. 42, no. 12, pp. 62–70, Dec. 2004.
- [14] Y. Pan *et al.*, "Message integrity protection over wireless channel: Counteracting signal cancellation via channel randomization," *IEEE Trans. Dependable Secure Comput.*, to be published.
- [15] *Service Requirements for the 5G System—Stage 1 (rel. 15)*, document TS 22.261, 3GPP, Dec. 2017. [Online]. Available: <http://www.3gpp.org/ftp//Specs/archive/22.261/22261-f30.zip>
- [16] *Study on Scenarios and Requirements for Next Generation Access Technologies*, document ETSI TR 138 913 v14.2.0, May 2017. [Online]. Available: http://www.etsi.org/deliver/etsi_tr/138900_138999/138913/14.02.00_60/tr_138913v140200p.pdf
- [17] H. Tullberg *et al.*, "The METIS 5G system concept: Meeting the 5G requirements," *IEEE Commun. Mag.*, vol. 54, no. 12, pp. 132–139, Dec. 2016.
- [18] *Future Technology Trends of Terrestrial IMT Systems*, document ITU-R M.2320-0, ITU-R, Nov 2014. [Online]. Available: https://www.itu.int/dms_pub/itu-r/opb/rep/R-REP-M.2320-2014-PDF-E.pdf
- [19] Z. Niu, Y. Wu, J. Gong, and Z. Yang, "Cell zooming for cost-efficient green cellular networks," *IEEE Commun. Mag.*, vol. 48, no. 11, pp. 74–79, Nov. 2010.
- [20] C. Y. Wang, C. H. Ko, H. Y. Wei, and A. V. Vasilakos, "A voting-based femtocell downlink cell-breathing control mechanism," *IEEE/ACM Trans. Netw.*, vol. 24, no. 1, pp. 85–98, Feb. 2016.
- [21] A. Tall, Z. Altman, and E. Altman, "Virtual sectorization: Design and self-optimization," in *Proc. IEEE 81st Veh. Technol. Conf. (VTC Spring)*, May 2015, pp. 1–5.
- [22] G. H. Huff, J. Feng, S. Zhang, and J. T. Bernhard, "A novel radiation pattern and frequency reconfigurable single turn square spiral microstrip antenna," *IEEE Microw. Wireless Compon. Lett.*, vol. 13, no. 2, pp. 57–59, Feb. 2003.
- [23] L. Petit, L. Dussart, and J. M. Laheurte, "MEMS-switched parasitic-antenna array for radiation pattern diversity," *IEEE Trans. Antennas Propag.*, vol. 54, no. 9, pp. 2624–2631, Sep. 2006.
- [24] S. Zhang, G. H. Huff, J. Feng, and J. T. Bernhard, "A pattern reconfigurable microstrip parasitic array," *IEEE Trans. Antennas Propag.*, vol. 52, no. 10, pp. 2773–2776, Oct. 2004.
- [25] X.-S. Yang, B.-Z. Wang, and Y. Zhang, "Pattern-reconfigurable quasi-yagi microstrip antenna using a photonic band gap structure," *Microw. Opt. Technol. Lett.*, vol. 42, no. 4, pp. 296–297, 2004, doi: [10.1002/mop.20283](https://doi.org/10.1002/mop.20283).
- [26] S. Nikolaou, G. E. Ponchak, J. Papapolymerou, and M. M. Tentzeris, "Design and development of an annular slot antenna (ASA) with a reconfigurable radiation pattern," in *Proc. Asia-Pacific Microw. Conf.*, vol. 5, Dec. 2005, p. 3.
- [27] X.-S. Yang, B.-Z. Wang, and W. Wu, "Pattern reconfigurable patch antenna with two orthogonal quasi-Yagi arrays," in *Proc. IEEE Antennas Propag. Soc. Int. Symp.*, vol. 2B, Jul. 2005, pp. 617–620.
- [28] C. W. Jung, M.-J. Lee, G. P. Li, and F. De Flaviis, "Reconfigurable scan-beam single-arm spiral antenna integrated with RF-MEMS switches," *IEEE Trans. Antennas Propag.*, vol. 54, no. 2, pp. 455–463, Feb. 2006.
- [29] J. C. Maloney *et al.*, "Switched fragmented aperture antennas," in *Proc. IEEE Antennas Propag. Soc. Int. Symp.*, vol. 1, Jul. 2000, pp. 310–313.
- [30] Z. Li, E. Ahmed, A. M. Eltawil, and B. A. Cetiner, "A beam-steering reconfigurable antenna for WLAN applications," *IEEE Trans. Antennas Propag.*, vol. 63, no. 1, pp. 24–32, Jan. 2015.
- [31] Z. Li, H. Mopidevi, O. Kaynar, and B. A. Cetiner, "Beam-steering antenna based on parasitic layer," *Electron. Lett.*, vol. 48, no. 2, pp. 59–60, Jan. 2012.
- [32] X. Yuan *et al.*, "A parasitic layer-based reconfigurable antenna design by multi-objective optimization," *IEEE Trans. Antennas Propag.*, vol. 60, no. 6, pp. 2690–2701, Jun. 2012.
- [33] G. Von Trentini, "Partially reflecting sheet arrays," *IRE Trans. Antennas Propag.*, vol. 4, no. 4, pp. 666–671, Oct. 1956.
- [34] A. P. Ferasidis and J. C. Vardaxoglou, "High gain planar antenna using optimised partially reflective surfaces," *IEE Proc.-Microw. Antennas Propag.*, vol. 148, no. 6, pp. 345–350, Dec. 2001.
- [35] A. R. Weily, T. S. Bird, and Y. J. Guo, "A reconfigurable high-gain partially reflecting surface antenna," *IEEE Trans. Antennas Propag.*, vol. 56, no. 11, pp. 3382–3390, Nov. 2008.
- [36] T. Debogovic, J. Bartolić, and J. Perrisseau-Carrier, "Array-fed partially reflective surface antenna with dynamic beamwidth control and beam-steering," in *Proc. 6th Eur. Conf. Antennas Propag. (EUCAP)*, Mar. 2012, pp. 3599–3603.
- [37] T. Debogovic and J. Perrisseau-Carrier, "Array-fed partially reflective surface antenna with independent scanning and beamwidth dynamic control," *IEEE Trans. Antennas Propag.*, vol. 62, no. 1, pp. 446–449, Jan. 2014.
- [38] 5GAmericas, (Apr. 2017). *5G Spectrum Recommendations*. [Online]. Available: http://www.5gamericas.org/files/9114/9324/1786/5GA_Spectrum_Recommendations_2017_FINAL.pdf
- [39] (Apr. 2015). *RESOLUTION 239(WRC-15): Studies Concerning Wireless Access Systems Including Radio Local Area Networks in the Frequency Bands Between 5150 MHz and 5925 MHz*. [Online]. Available: http://www.itu.int/dms_pub/itu-r/oth/0c/0a/R0COA00000C0017PDFE.pdf
- [40] D. M. Pozar, "Microstrip antenna aperture-coupled to a microstripline," *Electron. Lett.*, vol. 21, no. 1, pp. 49–50, Jan. 1985.
- [41] Rogers, Rogers Corp., Chandler, AZ, USA, 2016.
- [42] HFSS, Ansoft Corp., Pittsburgh, PA, USA, 2015.
- [43] S. Uda, "Wireless beam of short electric waves," *J. Inst. Elect. Eng.*, no. 452, pp. 273–282, Mar. 1926.
- [44] H. Yagi, "Beam transmission of ultra short waves," *Proc. IRE*, vol. 16, no. 6, pp. 715–740, Jun. 1928.
- [45] J. Huang, "Planar microstrip Yagi array antenna," in *Dig. Antennas Propag. Soc. Int. Symp.*, Jun. 1989, pp. 894–897.
- [46] J. Huang and A. C. Denmore, "Microstrip Yagi array antenna for mobile satellite vehicle application," *IEEE Trans. Antennas Propag.*, vol. 39, no. 7, pp. 1024–1030, Jul. 1991.
- [47] I. E. Rana, N. G. Alexopoulos, and P. L. Katehi, "Theory of microstrip Yagi-Uda arrays," *Radio Sci.*, vol. 16, no. 6, pp. 1077–1079, Nov./Dec. 1981.
- [48] W. L. Stutzman and G. A. Thiele, *Antenna Theory and Design*. Hoboken, NJ, USA: Wiley, 2012.
- [49] *NR—Physical Channels and Modulation (rel. 15)*, document TS 38.211, 3GPP, Sep. 2017. [Online]. Available: http://www.3gpp.org/ftp//Specs/archive/38_series/38.211/38211-100.zip
- [50] *Study on 3D Channel Model for LTE (Rel. 12)*, document TR 36.873, 3GPP, Jun. 2015. [Online]. Available: <http://www.3gpp.org/ftp/Specs/archive/36.873/36873-c20.zip>



Md. Asaduzzaman Towfig (S'11) received the B.S. degree in electrical and electronics engineering from the Bangladesh University of Engineering and Technology, Dhaka, Bangladesh, in 2013. He is currently pursuing the Ph.D. degree with Utah State University, Logan, Utah.

His current research interests include reconfigurable antenna, phased array and millimeter-wave antennas.



Israfil Bahceci (M'16) received the B.S. degree in electrical engineering from Bilkent University, Ankara, Turkey, in 1999, the M.S. degree in electrical engineering from Arizona State University, Tempe, AZ, USA, in 2001, and the Ph.D. degree in electrical engineering from the Georgia Institute of Technology, Atlanta, GA, USA, in 2005.

From 2005 to 2007, he was a Post-Doctoral Fellow with the University of Waterloo, Waterloo, ON, Canada. From 2007 to 2009, he was a Research and Development Engineer with Nortel Networks, Inc., Mississauga, ON. From 2009 to 2011, he was with Huawei Technologies, Markham, ON. From 2011 to 2015, he was with the TOBB University of Economics and Technology, Ankara. From 2015 to 2017, he was a Research Scientist with the Department of Electrical and Computer Engineering, Utah State University, Logan, UT, USA. He is currently with Ericsson Canada Inc., Ottawa, ON. His current research interests include systems, with a particular focus on communication and signal processing, wireless and mobile communications, distributed estimation/detection, and reconfigurable antenna systems for 5G and beyond systems.



Sebastián Blanch was born in Barcelona, Spain, in 1961. He received the Ing. and Dr.Ing. degrees in telecommunication engineering from the Universitat Politcnica de Catalunya (UPC), Barcelona, in 1989 and 1996, respectively.

In 1989, he joined the Electromagnetic and Photonics Engineering Group, Signal Theory and Communications Department, UPC. He is currently an Associate Professor with UPC. His current research interests include antenna near-field measurements, antenna diagnostics, and antenna design.



Lluís Jofre (F'10) was born in Canet de Mar, Spain, in 1956. He received the M.Sc. and Ph.D. degrees in electrical engineering (telecommunication engineering) from the Universitat Politcnica de Catalunya (UPC), Barcelona, Spain, in 1978 and 1982, respectively.

From 1979 to 1980, he was a Research Assistant with the Electrophysics Group, UPC, where he was involved in the analysis and near-field measurement of antennas and scatterers. From 1981 to 1982, he was with the Ecole Suprieure dElectricit Paris, Gif-sur-Yvette, France, where he was involved in microwave antenna design and imaging techniques for medical and industrial applications. Since 1982, he has been with the Communications Department, Telecommunication Engineering School, UPC, as an Associate Professor and then has been a full Professor since 1989. From 1986 to 1987, he was a Visiting Fulbright Scholar with the Georgia Institute of Technology, Atlanta, GA, USA, where he was involved in antenna near-field measurements and electromagnetic imaging. From 1989 to 1994, he was the Director of the Telecommunication Engineering School, UPC, and from 1994 to 2000, he was the UPC Vice-Rector for academic planning. From 2000 to 2001, he was a Visiting Professor with the Electrical and Computer Engineering Department, Henry Samueli School of Engineering, University of California at Irvine, Irvine, CA, USA, where he was involved in reconfigurable antennas and microwave sensing of civil engineering structures. He was the Director of the Catalan Research Foundation from 2002 to 2004 and the Director of the UPC-Telefonica Chair on Information Society Future Trends since 2003. He was a Principal Investigator of the 2008–2013 Spanish Sensing Lab Consolider Project, the General Director and then Secretary for Catalan Universities and Research from 2011 to 2016, and a Research Leader of the 2017–2020 ComSense Lab Maria de Maeztu Project. He has authored more than 200 scientific and technical papers, reports, and chapters in specialized volumes. His current research interests include antennas, electromagnetic scattering and imaging, system miniaturization for wireless, and sensing industrial and bio-applications from microwaves to terahertz frequencies.



Jordi Romeu (F'12) was born in Barcelona, Spain, in 1962. He received the Ing.de Telecomunicacin and Dr. Ing.de Telecommunicacon degrees from the Universitat Politcnica de Catalunya (UPC), Barcelona, in 1986 and 1991, respectively.

Since 1985, he has been with the Electromagnetic and Photonic Engineering Group, Signal Theory and Communications Department, UPC, where he is currently a full Professor and involved in the research of antenna near-field measurements, antenna diagnostics, and antenna design. In 1999, he joined the Antenna Laboratory, University of California at Los Angeles, Los Angeles, CA, USA, as a Visiting Scholar, under the North Atlantic Treaty Organization Scientific Program Scholarship. In 2004, he joined the University of California at Irvine, Irvine, CA, USA. He has authored 50 refereed papers in international journals and 50 conference proceedings. He holds several patents.

Dr. Romeu was a recipient of the Grand Winner of the European IT Prize by the European Commission in 1998, for his contributions in the development of fractal antennas.



Bedri A. Cetiner (M'99–SM'18) was a North Atlantic Treaty Organization Science Fellow with the University of California at Los Angeles, Los Angeles, CA, USA, from 1999 to 2000. From 2000 to 2004, he was a Research Scientist with the Electronics and Communication Engineering Department, University of California at Irvine, Irvine, CA, USA. From 2004 to 2007, he was an Assistant Professor with the Department of Space Science and Engineering, Morehead State University, Morehead, KY, USA. In 2007, he joined Utah State University, Logan, UT, USA, where he is currently a Professor with the Department of Electrical Engineering. He is also a Founder, President, and CEO of i5 Technologies Inc., Logan, UT, USA. He is the Principal Inventor of nine patented technologies in the area of wireless communications. His current research interests include the applications of micro- and nanotechnologies to a new class of microwave/millimeter-wave circuits and systems, and intelligent wireless communications systems with an emphasis on multifunctional reconfigurable antenna equipped MIMO systems.